

OccNeRF: Advancing 3D Occupancy Prediction in LiDAR-Free Environments

Chubin Zhang^{1*}, Juncheng Yan^{1*}, Yi Wei^{1,2*},
Jiaxin Li³, Li Liu⁴, Yansong Tang^{1†}, Yueqi Duan¹, and Jiwen Lu^{1,2}

¹ Tsinghua University

² Beijing National Research Center for Information Science and Technology

³ Gaussian Robotics

⁴ Xiaomi Car

Abstract. As a fundamental task of vision-based perception, 3D occupancy prediction reconstructs 3D structures of surrounding environments. It provides detailed information for autonomous driving planning and navigation. However, most existing methods heavily rely on the LiDAR point clouds to generate occupancy ground truth, which is not available in the vision-based system. In this paper, we propose an OccNeRF method for training occupancy networks without 3D supervision. Different from previous works which consider a bounded scene, we parameterize the reconstructed occupancy fields and reorganize the sampling strategy to align with the cameras' infinite perceptive range. The neural rendering is adopted to convert occupancy fields to multi-camera depth maps, supervised by multi-frame photometric consistency. Moreover, for semantic occupancy prediction, we design several strategies to polish the prompts and filter the outputs of a pretrained open-vocabulary 2D segmentation model. Extensive experiments for both self-supervised depth estimation and 3D occupancy prediction tasks on nuScenes and SemanticKITTI datasets demonstrate the effectiveness of our method. Code is available at <https://github.com/LinShan-Bin/OccNeRF>.

Keywords: 3D occupancy prediction · LiDAR-free · depth estimation

1 Introduction

Recent years have witnessed the great process of autonomous driving [43, 45, 53, 88]. As a crucial component, 3D perception helps the model to understand the real 3D world. Although LiDAR provides a direct means to capture geometric data, its adoption is hindered by the expense of sensors and the sparsity of scanned points. In contrast, as a cheap while effective solution, the vision-centric methods [1, 30, 48, 53, 54, 97] have received more and more attention. Among various 3D scene understanding tasks, multi-camera 3D object detection [31, 43, 45, 52] plays an important role in autonomous systems. However, it struggles to detect objects from infinite classes and suffers from long-tail problems as illustrated in [88, 94].

* Equal contribution.

† Corresponding author.

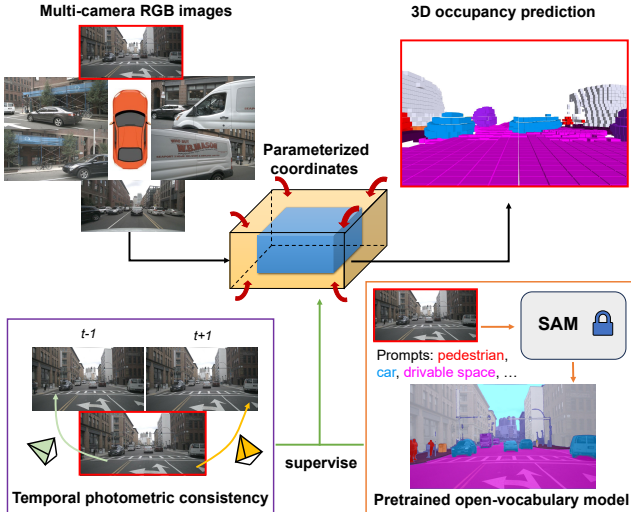


Fig. 1: The overview of OccNeRF. To represent unbounded scenes, we propose a parameterized coordinate to contract infinite space to the bounded occupancy fields. Without using any LiDAR data or annotated labels, we leverage temporal photometric constraints and pretrained open-vocabulary segmentation models to provide geometric and semantic supervision.

Complementary to 3D object detection, 3D occupancy prediction [9,77,83,96] reconstructs the geometric structure of surrounding scenes directly, which naturally alleviates the problems mentioned above. As mentioned in [88], 3D occupancy is a good 3D representation for multi-camera scene reconstruction since it has the potential to reconstruct occluded parts and guarantees multi-camera consistency. Recently, some methods have been proposed to lift image features to the 3D space and further predict 3D occupancy. However, most of these methods need 3D occupancy labels for supervision. While some previous research [77,88] has employed multi-frame LiDAR point accumulation to automatically label occupancy ground truth, the volume of LiDAR data is significantly less than that of image data. Collecting LiDAR data requires specialized vehicles equipped with LiDAR sensors, which is costly. Moreover, this approach neglects a vast quantity of unlabeled multi-camera image data. Consequently, investigating LiDAR-free methods for training occupancy presents a promising research avenue.

To address this, we propose an OccNeRF method, which targets at training multi-camera occupancy networks without 3D supervision. The overview of our proposed method is shown in Fig. 1. We first utilize a 2D backbone to extract multi-camera 2D features. To save memory, we directly interpolate 2D features to obtain 3D volume features instead of using heavy cross-view attention. In previous works, the volume features are supervised by the bounded occupancy labels (*e.g.* 50m range) and they only need to predict the occupancy with finite resolution (*e.g.* $200 \times 200 \times 16$). Differently, for LiDAR-free training, we should consider unbounded scenes since the RGB images perceive an infinite range. To

this end, we parameterize the occupancy fields to represent unbounded environments. Specifically, we split the whole 3D space into the inside and outside regions. The inside one maintains the original coordinate while the outside one adopts a contracted coordinate. A specific sampling strategy is designed to transfer parameterized occupancy fields to 2D depth maps with neural rendering.

A straightforward way to supervise predicted occupancy is to calculate loss between rendered images and training images, which is the same as the loss function used in NeRF [59]. However, our experiments indicate this method’s ineffectiveness due to the sparse nature of surrounding views, where minimal image overlap fails to supply sufficient geometric information. As an alternative, we take full advantage of temporal information by rendering multiple frames in a sequence and employing photometric consistency between adjacent frames as the primary supervision signal. For semantic occupancy, we propose three strategies to map the class names to the prompts, which are fed to a pretrained open-vocabulary segmentation model [36, 51] to get 2D semantic labels. Then an additional semantic head is employed to render semantic images and supervised by these labels. To verify the effectiveness of our method, we conduct experiments on both self-supervised multi-camera depth estimation and 3D occupancy prediction tasks. Experimental results show that our OccNeRF outperforms other depth estimation methods by a large margin and achieves comparable performance with some methods using stronger supervision on the nuScenes [8] and SemanticKITTI [5] datasets.

In summary, our key contributions are:

- We design a system that trains an occupancy network without LiDAR data, addressing the challenge of sparse surrounding views through the incorporation of temporal information.
- We introduce the parameterized occupancy field that allows vision-centric systems to efficiently represent unbounded scenes, matching the extensive perceptual range of cameras.
- We devise three strategies to improve the quality of pseudo labels generated by pretrained open-vocabulary segmentation models.

2 Related Work

2.1 3D Occupancy Prediction

Due to the significance of the vision-centric autonomous driving systems, more and more researchers begin to focus on 3D occupancy prediction tasks [9, 10, 28, 32, 42, 46, 47, 77, 78, 83, 88, 96, 102]. In the industry community, 3D occupancy is treated as an alternative to LiDAR perception. As one of the pioneering works, MonoScene [9] extracts the voxel features generated by sight projection to reconstruct scenes from a single image. TPVFormer [32] further extends it to multi-camera fashion with tri-perspective view representation. Beyond TPVFormer, SurroundOcc [88] designs a pipeline to generate dense occupancy labels instead of using sparse LiDAR points as the ground truth. In addition, a

2D-3D UNet with cross-view attention layers is proposed to predict dense occupancy. RenderOcc [63] uses the 2D depth maps and semantic labels to train the model, reducing the dependence on expensive 3D occupancy annotations. Compared with these methods, our method does not need any annotated 3D or 2D labels. Recently, as a preprint work, SimpleOccupancy [19] presents a simple while effective framework for occupancy estimation. Although SimpleOccupancy investigates the vision-centric setting, it does not consider the infinite range and semantic prediction.

2.2 Neural Radiance Fields

As one of the most popular topics in 3D area, neural radiance fields (NeRF) [7, 12, 16, 34, 39, 49, 56, 58, 61, 74, 76, 84, 90] have made great achievement in recent years. NeRF [59] learns the geometry of a scene by optimizing a continuous volumetric scene function with multi-view images. To obtain the novel views, volume rendering is performed to convert the radiance fields to RGB images. As a follow-up, mip-NeRF [2] represents the scene at a continuously valued and replaces rays as anti-aliased conical frustums. Beyond mip-NeRF, Zip-NeRF [4] integrates mip-NeRF with a grid-based model for faster training and better quality. There are several extensions of original NeRF, including dynamic scenes [21, 44, 64, 65, 80], model accelerating [62, 82, 86, 91, 93], 3D reconstruction [11, 17, 22, 60, 67, 75], etc. As one of these extensions, some works aim to describe unbounded scenes [3, 95]. NeRF++ [95] split the 3D space as an inner unit sphere and an outer volume and proposes inverted sphere parameterization to represent outside regions. Further, mip-NeRF 360 [3] embeds this idea into mip-NeRF and applies the smooth parameterization to volumes. Inspired by these methods, we also design a parameterization scheme to model the unbounded scene for occupancy prediction.

2.3 Self-supervised Depth Estimation

While early works [18, 38, 50, 69, 98] require dense depth annotations, recent depth estimation methods [6, 14, 25, 37, 55, 66, 71, 72, 79, 81, 85, 92, 99, 101] are designed in a self-supervised manner. Most of these methods predict depth maps and ego-motions simultaneously, adopting the photometric constraints [23, 100] between successive frames as the supervision signal. As a classical work in this field, Monodepth2 [24] proposes some techniques to improve the quality of depth predictions, including the minimum re-projection loss, full-resolution multi-scale sampling, and auto-masking loss. Since modern self-driving vehicles are usually equipped with multiple cameras to capture the surrounding views, researchers begin to concentrate on the multi-camera self-supervised depth estimation task [26, 35, 70, 73, 87, 89]. FSM [26] is the first work to extend monocular depth estimation to full surrounding views by leveraging spatiotemporal contexts and pose consistency constraints. To predict the real-world scale, Surround-Depth [87] uses structure-from-motion to generate scale-aware pseudo depths to pretrain the models. Further, it proposes the cross-view transformer and joint pose estimation to incorporate the multi-camera information. Recently,

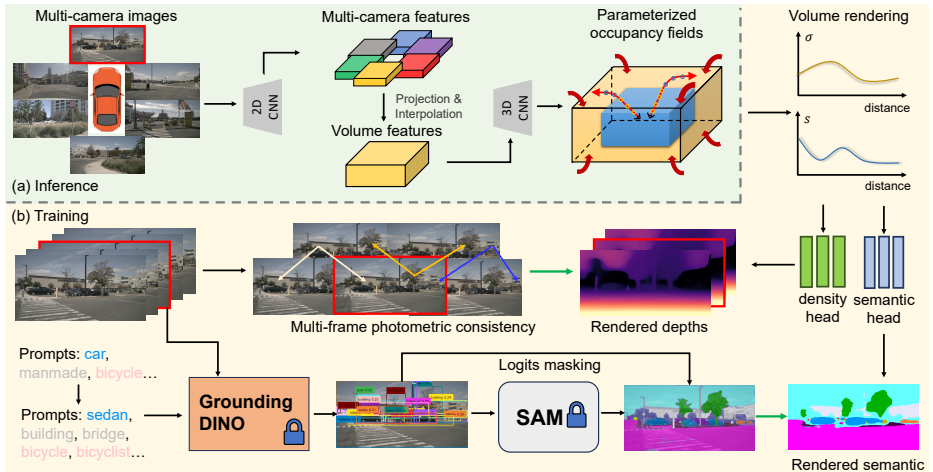


Fig. 2: The pipeline of OccNeRF. (a) At inference time, we first use a 2D backbone to extract multi-camera features, which are lifted to 3D space to get volume features with projection and interpolation. The parameterized occupancy fields are reconstructed to describe unbounded scenes. (b) To obtain the rendered depth and semantic maps during training, we perform volume rendering with our reorganized sampling strategy. The multi-frame depths are supervised by photometric loss. For semantic prediction, we adopted pretrained Grounded-SAM with prompts cleaning. The green arrow indicates supervision signals.

R3D3 [70] combines the feature correlation with bundle adjustment operators for robust depth and pose estimation. Different from these methods, our approach directly extracts features in 3D space, achieving multi-camera consistency and better reconstruction quality.

3 Approach

3.1 Overview

Fig. 2 shows the pipeline of our approach. With the multi-camera images $\{I^i\}_{i=1}^N$ as inputs, we first utilize a 2D backbone to extract N cameras' features $\{X^i\}_{i=1}^N$. Then the 2D features are interpolated to the 3D space to obtain the volume features with known intrinsic $\{K^i\}_{i=1}^N$ and extrinsic $\{T^i\}_{i=1}^N$. As discussed in Section 3.2, to represent the unbounded scenes, we propose a coordinate parameterization to contract the infinite range to a limited occupancy field. The volume rendering is performed to convert occupancy fields to multi-frame depth maps, which are supervised by photometric loss. Section 3.3 introduces this part in detail. Finally, Section 3.4 shows how we use a pretrained open-vocabulary segmentation model to get 2D semantic labels.

3.2 Parameterized Occupancy Fields

Different from previous works [88, 96], we need to consider unbounded scenes in the LiDAR-free setting. On the one hand, we should preserve high resolution for

the inside region (e.g. [-40m, -40m, -1m, 40m, 40m, 5.4m]), since this part covers most regions of interest. On the other hand, the outside region is necessary but less informative and should be represented within a contracted space to reduce memory consumption. Inspired by [3], we propose a transformation function with adjustable regions of interest and contraction threshold to parameterize the coordinates $r = (x, y, z)$ of each voxel grid:

$$f(r) = \begin{cases} \alpha \cdot r' & |r'| \leq 1 \\ \frac{r'}{|r'|} \cdot \left(1 - \frac{(1-\alpha)^2}{\alpha|r'|-2\alpha+1}\right) & |r'| > 1 \end{cases}, \quad (1)$$

where $r' = r/r_b$ is the normalized coordinate of the input r and $f(r) \in (-1, 1)$ indicates the normalized parameterized coordinate. r_b is the bound of the inside region, which is different for x, y, z directions. $\alpha \in [0, 1]$ represents the proportion of the region of interest in the parameterized space. Higher α indicates we use more space to describe the inside region. Note that the two functions in Equation 1 have the same value and gradient at $r = r_b$. Please refer to the supplementary material for the derivation details.

To obtain 3D voxel features from 2D views, we first generate the corresponding points $\mathcal{P}_{pc} = [\mathbf{x}_{pc}, \mathbf{y}_{pc}, \mathbf{z}_{pc}]^T$ for each voxel in the parameterized coordinate system and map them back to the ego coordinate system:

$$\mathcal{P} = [f_x^{-1}(\mathbf{x}_{pc}), f_y^{-1}(\mathbf{y}_{pc}), f_z^{-1}(\mathbf{z}_{pc})]^T. \quad (2)$$

Then we project these points to the 2D image feature planes and use bilinear interpolation to get the 2D features:

$$\mathcal{F}^i = X^i \langle \text{proj}(\mathcal{P}, T^i, K^i) \rangle. \quad (3)$$

where proj is the function projecting 3D points \mathcal{P} to the 2D image plane defined by the camera extrinsic T^i and intrinsic K^i , $\langle \rangle$ is the bilinear interpolation operator, \mathcal{F}^i is the interpolation result. To simplify the aggregation process and reduce computation costs, we directly average the multi-camera 2D features to get volume features, which is the same as the method used in [19, 27]. Finally, a 3D convolution network [20] is employed to extract features and predict final occupancy outputs.

3.3 Multi-frame Depth Estimation

To project the occupancy fields to multi-camera depth maps, we adopt volume rendering [57], which is widely used in NeRF-based methods [2, 59, 95]. To render the depth value of a given pixel, we cast a ray from the camera center \mathbf{o} along the direction \mathbf{d} pointing to the pixel. The ray is represented by $\mathbf{v}(t) = \mathbf{o} + t\mathbf{d}$, $t \in [t_n, t_f]$. Then, we sample L points $\{t_k\}_{k=1}^L$ along the ray in 3D space to get the density $\sigma(t_k)$. For the selected L quadrature points, the depth of the corresponding pixel is computed by:

$$D(\mathbf{v}) = \sum_{k=1}^L T(t_k)(1 - \exp(-\sigma(t_k)\delta_k))t_k, \quad (4)$$

where $T(t_k) = \exp\left(-\sum_{k'=1}^{k-1} \sigma(t_k)\delta_k\right)$, and $\delta_k = t_{k+1} - t_k$ are intervals between sampled points.

A vital problem here is how to sample $\{t_k\}_{k=1}^L$ in our proposed coordinate system. Uniform sampling in the depth space or disparity space will result in an unbalanced series of points in either the outside or inside region of our parameterized grid, which is to the detriment of the optimization process. With the assumption that o is around the coordinate system’s origin, we directly sample $L(\mathbf{r})$ points from $U[0, 1]$ in parameterized coordinate and use the inverse function of Equation 1 to calculate the $\{t_k\}_{k=1}^{L(\mathbf{v})}$ in the ego coordinates. The specific $L(\mathbf{v})$ and $r_b(\mathbf{v})$ for a ray are calculated by:

$$r_b(\mathbf{v}) = \frac{\sqrt{(\mathbf{d} \cdot \mathbf{i}l_x)^2 + (\mathbf{d} \cdot \mathbf{j}l_y)^2 + (\mathbf{d} \cdot \mathbf{k}l_z)^2}}{2\|\mathbf{d}\|}, \quad (5)$$

$$L(\mathbf{v}) = \frac{2r_b(\mathbf{v})}{\alpha d_v}$$

where $\mathbf{i}, \mathbf{j}, \mathbf{k}$ are the unit vectors in the x, y, z directions, l_x, l_y, l_z are the lengths of the inside region, and d_v is the voxel size. To better adapt to the occupancy representation, we directly predict the rendering weight instead of the density.

A conventional supervision method is to calculate the difference between rendered images and raw images, which is employed in NeRF [59]. However, our experimental results show that it does not work well. The possible reason is that the large-scale scene and few view supervision make it difficult for NeRF to converge. To better make use of temporal information, we employ the photometric loss proposed in [24, 100]. Specifically, we project adjacent frames to the current frames according to the rendered depths and given relative poses. Then we calculate the reconstruction error between projected images and raw images:

$$\mathcal{L}_{pe}^i = \frac{\beta}{2}(1 - \text{SSIM}(I^i, \hat{I}^i)) + (1 - \beta)\|I^i, \hat{I}^i\|_1, \quad (6)$$

where \hat{I}^i is the projected image and $\beta = 0.85$. Moreover, we adopt the techniques introduced in [24], *i.e.* per-pixel minimum reprojection loss and auto-masking stationary pixels. For each camera view, we render a short sequence instead of a single frame and perform multi-frame photometric loss.

3.4 Semantic Supervision

To enhance the richness of occupancy voxel information and facilitate comparison with existing methods, we introduce 2D labels to provide semantic supervision. Previous works [41, 77] project 3D LiDAR points with segmentation labels to the image space to avoid the expensive cost of annotating dense 3D occupancy. However, we aim to predict semantic occupancy in a fully vision-centric system and use 2D data only. To this end, we leverage a pretrained open-vocabulary model Grounded-SAM [33, 36, 51] to generate 2D semantic segmentation labels. Without any 2D or 3D ground truth data, the pretrained open-vocabulary model

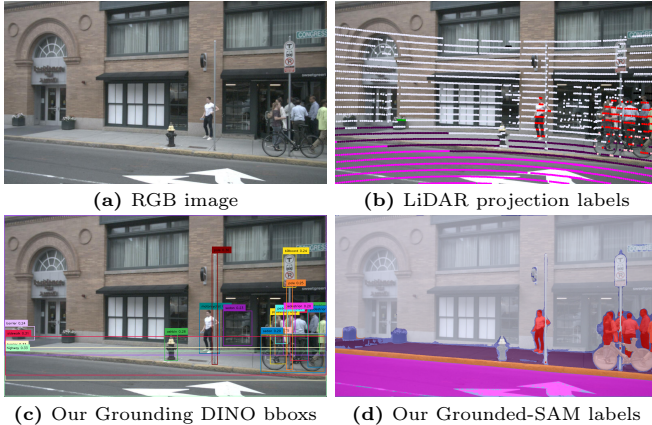


Fig. 3: Detection bounding boxes generated by our Grounding DINO and semantic labels predicted by SAM in our method exhibit precision, which is comparable with that of LiDAR points projection labels.

enables us to obtain 2D labels which closely match the semantics of the given category names. This method can easily extend to any dataset, making our approach efficient and generalizable.

Specifically, when dealing with c categories, we employ three strategies to determine the prompts provided to the Grounding DINO. These strategies consist of synonymous substitution, where we replace words with their synonyms (e.g., changing ‘car’ to ‘sedan’ to enable the model to distinguish it from ‘truck’ and ‘bus’); splitting single words into multiple entities (e.g., ‘manmade’ is divided into ‘building’, ‘billboard’, and ‘bridge’ etc. to enhance differentiation); and incorporating additional information (e.g., introducing ‘bicyclist’ to facilitate the detection of a person on a bike). Subsequently, we obtain detection bounding boxes along with their corresponding logits and phrases, which are fed to SAM [36] to generate M precise segmentation binary masks. After multiplying the Grounding DINO logits with binary masks, every pixel has $\{l_i\}_{i=1}^M$ logits. We get the per-pixel label \mathcal{S}^{pix} using:

$$\mathcal{S}^{pix} = \psi(\arg \max_i l_i), \quad (7)$$

where $\psi(\cdot)$ is a function that maps the index of l_i to the category label according to the phrases. If a pixel does not belong to any categories and gets M zero logits, we will give it an ‘uncertain’ label. The generated detection bounding boxes and semantic labels are shown in Fig. 3.

To leverage the 2D semantic supervision, we initially utilize a semantic head with c output channels to map volume features extracted to semantic outputs, denoted as $S(x)$. Similar to the method outlined in Section 3.3, we engage in volume rendering once more using the subsequent equation:

$$\hat{\mathcal{S}}^{pix}(\mathbf{r}) = \sum_{k=1}^{L_s} T(t_k)(1 - \exp(-\sigma(t_k)\delta_k))S(t_k), \quad (8)$$

where $\hat{\mathcal{S}}^{pix}$ represents the per-pixel semantic rendering output. To save the memory and improve efficiency, we do not render the pixels that are assigned with ‘uncertain’ labels. Moreover, we only render the central frame instead of multiple frames and reduce the sample ratio to $L_s = L/4$. Our overall loss function is expressed as:

$$\mathcal{L}_{total} = \sum_i \mathcal{L}_{pe}^i + \lambda \mathcal{L}_{sem}^i(\hat{\mathcal{S}}^{pix}, \mathcal{S}^{pix}) \quad (9)$$

where \mathcal{L}_{sem} is the cross-entropy loss function and λ is the semantic loss weight.

4 Experiments

4.1 Experimental Setup

Dataset: Our experiments are conducted on nuScenes [8] and SemanticKITTI [5] datasets. NuScenes [8] is a large-scale autonomous driving dataset which contains 600 scenes for training, 150 scenes for validation, and 150 for testing. The dataset has about 40000 frames and 17 classes in total. For self-supervised depth estimation, we project LiDAR point clouds to each view to get depth ground truth for evaluation. Following SurroundDepth [87], we clip the depth prediction and ground truth from 0.1m to 80m. To evaluate the semantic occupancy prediction, we use Occ3D-nuScenes [77] benchmark. The range of each sample is [-40 m, -40 m, -1 m, 40 m, 40 m, 5.4 m] and the voxel size is 0.4 m. Among 17 classes, we do not consider ‘other’ and ‘other flat’ classes for evaluation since open-vocabulary models cannot recognize the semantic-ambiguous text. Following [77, 87], we evaluate models on validation sets. Additionally, we explore 3D occupancy prediction using the SemanticKITTI [5] dataset. SemanticKITTI [5] is composed of 22 sequences (10 for training, 1 for validation and 11 for test) of scans and each scan contains voxelized LiDAR data and corresponding stereo images. The range of each sample is [-25.6 m, 0, -2.0 m, 25.6 m, 51.2 m, 4.4 m] and the voxel size is 0.2 m.

Implementation Details: We adopt ResNet-101 [29] with ImageNet [15] pre-trained weights as the 2D backbone to extract multi-camera features. For nuScenes [8], the predicted occupancy field has the shape 300x300x24. The central 200x200x16 voxels represent inside regions: -40m to 40m for the X and Y axis, and -1m to 5.4m for the Z axis, which is the same as the scope defined in Occ3D-nuScenes. For SemanticKITTI [5], the shape of the predicted occupancy field is 320x320x40. The central part is 256x256x32, also representing the scope defined by the dataset. We render 3 frame depth maps, which are supervised by the photometric loss with a sequence of 5 frame raw images (1 keyframe with 4 neighbored non-key frames). The α is set as 0.667. To predict semantic occupancy, the Grounded-SAM [36, 51] is employed as our pretrained open-vocabulary model. The text and box thresholds are set as 0.2 and we use the loss weight $\lambda = 0.05$. All experiments are conducted on 8 A100.

Table 1: Comparisons for self-supervised multi-camera depth estimation on the nuScenes dataset [8]. The results are averaged over all views without median scaling at test time. ‘FSM*’ is the reproduced result in [35].

Method	Abs Rel	Sq Rel	RMSE	RMSE log	$\delta < 1.25$	$\delta < 1.25^2$	$\delta < 1.25^3$
FSM [26]	0.297	-	-	-	-	-	-
FSM* [26]	0.319	7.534	7.860	0.362	0.716	0.874	0.931
SurroundDepth [87]	0.280	4.401	7.467	0.364	0.661	0.844	0.917
Kim <i>et al.</i> [35]	0.289	5.718	7.551	0.348	0.709	0.876	0.932
R3D3 [70]	0.253	4.759	7.150	-	0.729	-	-
SimpleOcc [19]	0.224	3.383	7.165	0.333	0.753	0.877	0.930
OccNeRF	0.202	2.883	6.697	0.319	0.768	0.882	0.931

Table 2: 3D Occupancy prediction performance on the Occ3D-nuScenes dataset [77]. ‘GT’ indicates occupancy ground truth. Since ‘other’ and ‘other flat’ classes are the invalid prompts for open-vocabulary models, we do not consider these two classes during evaluation. ‘mIoU*’ is the original result, and ‘mIoU’ is the result ignoring the classes.

Method	GT	mIoU		Classes														
		mIoU*	mIoU	barrier	bicycle	bus	car	const. veh.	motorcycle	pedestrian	traffic cone	trailer	truck	drive. suf.	sidewalk	terrain	manmade	vegetation
MonoScene [9]	✓	6.33	6.06	7.23	4.26	4.93	9.38	5.67	3.98	3.01	5.90	4.45	7.17	14.91	7.92	7.43	1.01	7.65
TPVFormer [32]	✓	28.69	27.83	38.90	13.67	40.78	45.90	17.23	19.99	18.85	14.30	26.69	34.17	55.65	37.55	30.70	19.40	16.78
BEVDet [31]	✓	20.03	19.38	30.31	0.23	32.26	34.47	12.97	10.34	10.36	6.26	8.93	23.65	52.27	26.06	22.31	15.04	15.10
OccFormer [96]	✓	22.39	21.93	30.29	12.32	34.40	39.17	14.44	16.45	17.22	9.27	13.90	26.36	50.99	34.66	22.73	6.76	6.97
BEVFormer [45]	✓	28.13	26.88	37.83	17.87	40.44	42.43	7.36	23.88	21.81	20.98	22.38	30.70	55.35	36.0	28.06	20.04	17.69
CTF-Occ [77]	✓	29.54	28.53	39.33	20.56	38.29	42.24	16.93	24.52	22.72	21.05	22.98	31.11	53.33	37.98	33.23	20.79	18.00
RenderOcc [63]	✓	24.53	23.93	27.56	14.36	19.91	20.56	11.96	12.42	12.14	14.34	20.81	18.94	68.85	42.01	43.94	17.36	22.61
SimpleOcc [19]	×	7.99	-	0.67	1.18	3.21	7.63	1.02	0.26	1.80	0.26	1.07	2.81	40.44	18.30	17.01	13.42	10.84
OccNeRF	×	10.81	-	0.83	0.82	5.13	12.49	3.50	0.23	3.10	1.84	0.52	3.90	52.62	20.81	24.75	18.45	13.19

4.2 Self-supervised Depth Estimation

Evaluation Metric: For depth estimation, we use the commonly used depth evaluation metrics [24, 87, 100]: Abs Rel, Sq Rel, RMSE, RMSE log and $\delta < t$. The Abs Rel is the main metric and see supplementary for the details of these metrics. During evaluation, we do not perform median scaling since our method can predict real-world scale. For 3D occupancy prediction, we use the mean intersection over union (mIoU) of all classes as the semantic-aware metric and intersection over union (IoU), precision and recall as semantic-agnostic metrics.

Table 1 shows the self-supervised multi-camera depth estimation results on nuScenes dataset. We do not use pretrained segmentation models in this experiment. The results are averaged over 6 cameras and ‘FSM*’ is the reproduced FSM [26] result reported in [35]. We can see that our method outperforms other SOTA methods by a large margin, demonstrating the effectiveness of OccNeRF. Compared with depth estimation methods, our method directly predicts occupancy in 3D space, naturally guaranteeing multi-camera consistency. Moreover, we do not need to lift 2D depth maps to 3D point clouds with post-processing.

Table 3: 3D Occupancy prediction performance on the SemanticKITTI dataset [5]. The results of other methods are from the table in SceneRF [10]. MonoScene* is supervised by depth predictions from [24]

Method	Supervision		IoU	Prec.	Rec.
	3D	Depth Image			
MonoScene [9]	✓		37.14	49.90	59.24
LMSCNet ^{rgb} [68]		✓	12.08	13.00	63.16
3DSketch ^{rgb} [13]		✓	12.01	12.95	62.31
AICNet ^{rgb} [40]		✓	11.28	11.84	70.89
MonoScene [9]		✓	13.53	16.98	40.06
MonoScene* [9]		✓	11.18	13.15	40.22
SceneRF [10]		✓	13.84	17.28	40.96
OccNeRF		✓	22.81	35.25	39.27

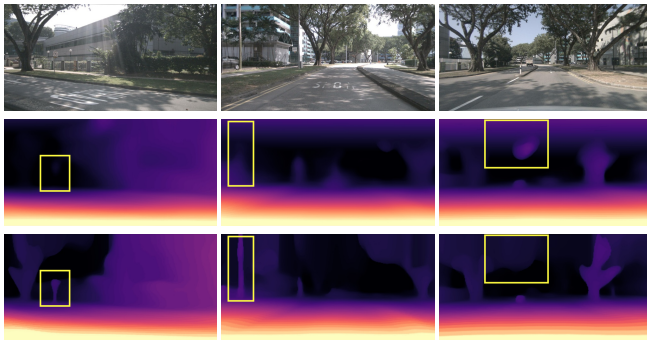


Fig. 4: Qualitative comparison of different coordinates. The second line indicates the results without using coordinate parameterization. With the ability to represent unbounded environments, our method can get better results in far scenes, such as the sky.

4.3 Semantic Occupancy Prediction

We conduct experiments on semantic occupancy prediction using the Occ3D-nuScenes dataset. The pretrained open-vocabulary model [36, 51] struggles with ambiguous prompts like 'other' and 'other flat', so we exclude them during the evaluation. To compare with the SimpleOcc method [19], we add a semantic head to the original model and leverage the generated 2D semantic labels to train it. Our approach significantly outperforms SimpleOcc, as detailed in Table 2, and achieves competitive results against some fully-supervised methods. Notably, it excels in predicting 'drivable space' and 'manmade' classes, outdoing all supervised methods. However, it falls short in detecting small objects, such as bicycles and pedestrians, where it lags behind state-of-the-art supervised methods, likely due to the open-vocabulary model's limitations in capturing small details.

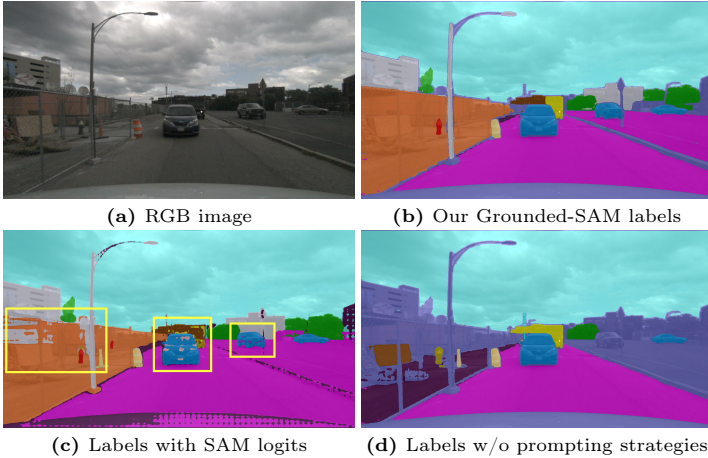


Fig. 5: Comparison of different semantic label generation methods. Compared with generating semantic labels with SAM logits or feeding raw category names, our semantic labels are preciser and have better continuity.

We further explored geometry occupancy prediction with the nuScenes [8] and SemanticKITTI [5]. Since most works reported in occ3D-nuScenes [77] do not provide codes, we can only evaluate RenderOcc [63] and SeimpleOcc [19]. As detailed in Table 3 and Table 7, our approach significantly outperforms other methods supervised by images and achieves competitive results against methods with even stronger supervision.

Table 4: The ablation study of supervision method. ‘Depth’ means whether we use the temporal photometric constraints to train the model. ‘Multi’ indicates whether we employ multi-frame rendering and supervision.

Depth	Multi	Abs Rel	RMSE	$\delta < 1.25$
		0.627	15.901	0.051
	✓	0.489	9.352	0.362
✓		0.216	6.752	0.764
✓	✓	0.202	6.697	0.768

Table 5: The ablation study of coordinate parameterization. ‘CC’ means whether we adopt contracted coordinates. ‘Resample’ indicates whether we leverage the proposed sampling strategy.

CC	Resample	Abs Rel	RMSE	$\delta < 1.25$
		0.216	8.465	0.694
✓		0.208	7.339	0.743
✓	✓	0.202	6.697	0.768

4.4 Ablation Study

Supervision Method: A straightforward supervision signal is a difference between the rendered and true pixel colours, which is the same as the loss function used in NeRF [59]. However, as shown in Table 4, this supervision method yields terrible performance. We attribute this to the challenge NeRF faces in learning

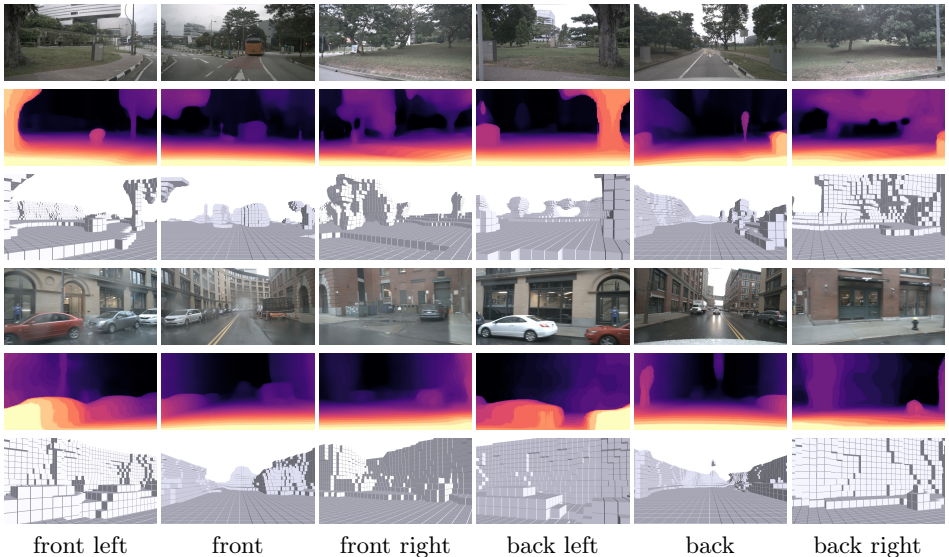


Fig. 6: Qualitative results on nuScenes dataset [8]. Our method can predict visually appealing depth maps with texture details and fine-grained occupancy. **Better viewed when zoomed in.**

the scene structure with only six views. On the contrary, temporal photometric loss (‘Depth’ in the table) can better leverage geometric cues in adjacent frames, which is the golden metric in self-supervised depth estimation methods. Moreover, multi-frame training provides stronger supervision, further boosting the model’s performance.

Coordinate Parameterization: Table 5 shows the ablation study of coordinate parameterization. Different from occupancy labels, the photometric loss assumes that the images perceive an infinite range. The contracted coordinate aims to represent the unbounded scene in a bounded occupancy. From the table, we can see that the contracted coordinate greatly improves the model’s performance. In addition, since the parameterized coordinate is not the Euclidean 3D space, the proposed sampling strategy works better than normal uniform sampling in the original ego coordinate.

Semantic Label Generation: In this subsection, we conduct ablation studies of semantic label generation on the nuScenes [8] dataset. First, we change grounding DINO [51] logits as SAM logits [36] to get semantic labels. As shown in Table 6 and Fig. 5, we find that the SAM logits are more noisy and discontinuous. Then, we also feed raw category names to the open-vocabulary model without proposed prompting strategies. However, this method leads to worse results since the original class names cannot provide fine-grained semantic guidance and bring ambiguity.

Table 6: The ablation study of semantic label generation. ‘SAM logits’ means that we directly use the logits from SAM [36]. ‘Category names’ means that we do not conduct the prompting strategies.

Method	mIoU
SAM logits	7.50
category names	8.23
Ours	10.81

Table 7: The scene reconstruction performance on the Occ3D-nuScenes dataset [77]. The results of other methods are reproduced with their released codes.

Method	GT	IoU	Prec.	Rec.
RenderOcc [63]	✓	53.09	59.97	82.23
SimpleOcc [19]	×	33.92	41.91	64.02
OccNeRF	×	39.20	57.20	55.47

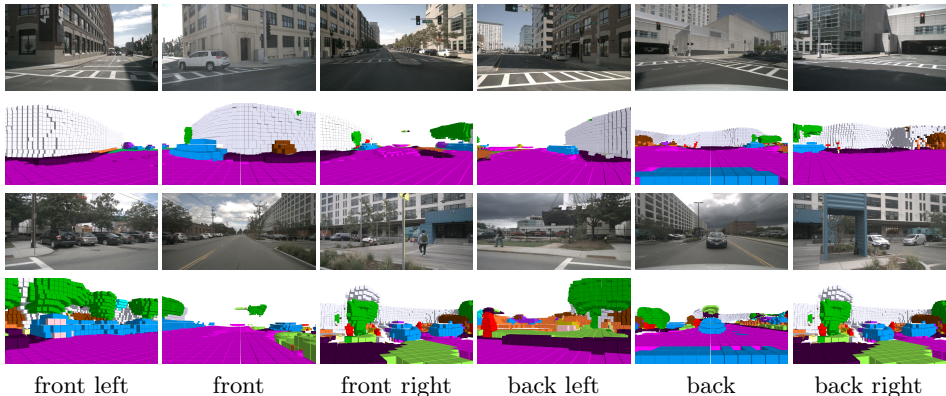


Fig. 7: Qualitative results of semantic occupancy on nuScenes dataset [8]. Our method can predict visually appealing semantic occupancy with well geometry correspondence. **Better viewed when zoomed in.**

4.5 Visualization

To further demonstrate the superiority of our method, we provide some qualitative results in Fig. 6 and 7. From Fig. 6, we can see that our method can generate high-quality depth maps and occupancy with fine-grained details. See supplementary material for more qualitative comparisons with other methods. For semantic occupancy prediction, as shown in Fig. 7, our OccNeRF can reconstruct dense results of the surrounding scenes, especially for the large-area categories, such as ‘drivable space’ and ‘manmade’.

5 Conclusion

In this paper, we propose OccNeRF for training multi-camera 3D occupancy without 3D supervision. To tackle the unbounded scenes, we propose the parameterized occupancy fields to contract the infinite space to a bounded voxel. To leverage temporal photometric loss, volume rendering is performed on parameterized coordinates to obtain multi-frame multi-camera depth maps. For the semantic occupancy prediction, we utilize an open-vocabulary model to get

2D semantic pseudo labels with the proposed prompt cleaning strategies. The experimental results on nuScenes and SemanticKITTI datasets demonstrate the effectiveness of our method. Future works include extending our approach to multi-frame inputs to enable occupancy flow prediction and reduce the reliance on open-vocabulary models for small objects prediction.

References

1. Akan, A.K., Güney, F.: Stretchbev: Stretching future instance prediction spatially and temporally. arXiv preprint arXiv:2203.13641 (2022)
2. Barron, J.T., Mildenhall, B., Tancik, M., Hedman, P., Martin-Brualla, R., Srinivasan, P.P.: Mip-nerf: A multiscale representation for anti-aliasing neural radiance fields. In: ICCV. pp. 5855–5864 (2021)
3. Barron, J.T., Mildenhall, B., Verbin, D., Srinivasan, P.P., Hedman, P.: Mip-nerf 360: Unbounded anti-aliased neural radiance fields. In: CVPR. pp. 5470–5479 (2022)
4. Barron, J.T., Mildenhall, B., Verbin, D., Srinivasan, P.P., Hedman, P.: Zip-nerf: Anti-aliased grid-based neural radiance fields. In: ICCV (2023)
5. Behley, J., Garbade, M., Milioto, A., Quenzel, J., Behnke, S., Stachniss, C., Gall, J.: Semantickitti: A dataset for semantic scene understanding of lidar sequences. In: Proceedings of the IEEE/CVF international conference on computer vision. pp. 9297–9307 (2019)
6. Bian, J.W., Li, Z., Wang, N., Zhan, H., Shen, C., Cheng, M.M., Reid, I.: Unsupervised Scale-consistent Depth and Ego-motion Learning from Monocular Video. In: NeurIPS. pp. 35–45 (2019)
7. Boss, M., Braun, R., Jampani, V., Barron, J.T., Liu, C., Lensch, H.: Nerf: Neural reflectance decomposition from image collections. In: ICCV. pp. 12684–12694 (2021)
8. Caesar, H., Bankiti, V., Lang, A.H., Vora, S., Liong, V.E., Xu, Q., Krishnan, A., Pan, Y., Baldan, G., Beijbom, O.: nuscenes: A multimodal dataset for autonomous driving. In: CVPR. pp. 11621–11631 (2020)
9. Cao, A.Q., de Charette, R.: Monoscene: Monocular 3d semantic scene completion. In: CVPR. pp. 3991–4001 (2022)
10. Cao, A.Q., de Charette, R.: Scenerf: Self-supervised monocular 3d scene reconstruction with radiance fields. In: ICCV. pp. 9387–9398 (2023)
11. Chen, A., Xu, Z., Geiger, A., Yu, J., Su, H.: Tensorf: Tensorial radiance fields. In: ECCV. pp. 333–350. Springer (2022)
12. Chen, A., Xu, Z., Zhao, F., Zhang, X., Xiang, F., Yu, J., Su, H.: Mvsnerf: Fast generalizable radiance field reconstruction from multi-view stereo. In: ICCV. pp. 14124–14133 (2021)
13. Chen, X., Lin, K.Y., Qian, C., Zeng, G., Li, H.: 3d sketch-aware semantic scene completion via semi-supervised structure prior. In: Proceedings of the IEEE/CVF Conference on Computer Vision and Pattern Recognition. pp. 4193–4202 (2020)
14. Chen, Y., Schmid, C., Sminchisescu, C.: Self-supervised learning with geometric constraints in monocular video: Connecting flow, depth, and camera. In: ICCV. pp. 7063–7072 (2019)
15. Deng, J., Dong, W., Socher, R., Li, L.J., Li, K., Fei-Fei, L.: Imagenet: A large-scale hierarchical image database. In: CVPR. pp. 248–255 (2009)

16. Deng, K., Liu, A., Zhu, J.Y., Ramanan, D.: Depth-supervised nerf: Fewer views and faster training for free. In: CVPR. pp. 12882–12891 (2022)
17. Fridovich-Keil, S., Yu, A., Tancik, M., Chen, Q., Recht, B., Kanazawa, A.: Plenoxels: Radiance fields without neural networks. In: CVPR. pp. 5501–5510 (2022)
18. Fu, H., Gong, M., Wang, C., Batmanghelich, K., Tao, D.: Deep ordinal regression network for monocular depth estimation. In: CVPR. pp. 2002–2011 (2018)
19. Gan, W., Mo, N., Xu, H., Yokoya, N.: A simple attempt for 3d occupancy estimation in autonomous driving. arXiv preprint arXiv:2303.10076 (2023)
20. Gan, W., Wu, W., Chen, S., Zhao, Y., Wong, P.K.: Rethinking 3d cost aggregation in stereo matching. *Pattern Recognition Letters* **167**, 75–81 (2023)
21. Gao, C., Saraf, A., Kopf, J., Huang, J.B.: Dynamic view synthesis from dynamic monocular video. In: ICCV. pp. 5712–5721 (2021)
22. Garbin, S.J., Kowalski, M., Johnson, M., Shotton, J., Valentin, J.: Fastnerf: High-fidelity neural rendering at 200fps. In: ICCV. pp. 14346–14355 (2021)
23. Godard, C., Mac Aodha, O., Brostow, G.J.: Unsupervised monocular depth estimation with left-right consistency. In: CVPR. pp. 270–279 (2017)
24. Godard, C., Mac Aodha, O., Firman, M., Brostow, G.J.: Digging into self-supervised monocular depth estimation. In: ICCV. pp. 3828–3838 (2019)
25. Guizilini, V., Ambrus, R., Pillai, S., Raventos, A., Gaidon, A.: 3d packing for self-supervised monocular depth estimation. In: CVPR. pp. 2485–2494 (2020)
26. Guizilini, V., Vasiljevic, I., Ambrus, R., Shakhnarovich, G., Gaidon, A.: Full surround monodepth from multiple cameras. *RAL* **7**(2), 5397–5404 (2022)
27. Harley, A.W., Fang, Z., Li, J., Ambrus, R., Fragkiadaki, K.: Simple-BEV: What really matters for multi-sensor bev perception? In: IEEE International Conference on Robotics and Automation (ICRA) (2023)
28. Hayler, A., Wimbauer, F., Muhle, D., Rupperecht, C., Cremers, D.: S4c: Self-supervised semantic scene completion with neural fields. arXiv preprint arXiv:2310.07522 (2023)
29. He, K., Zhang, X., Ren, S., Sun, J.: Deep residual learning for image recognition. In: CVPR. pp. 770–778 (2016)
30. Hu, A., Murez, Z., Mohan, N., Dudas, S., Hawke, J., Badrinarayanan, V., Cipolla, R., Kendall, A.: Fiery: Future instance prediction in bird’s-eye view from surround monocular cameras. In: ICCV. pp. 15273–15282 (2021)
31. Huang, J., Huang, G., Zhu, Z., Du, D.: Bevdet: High-performance multi-camera 3d object detection in bird-eye-view. arXiv preprint arXiv:2112.11790 (2021)
32. Huang, Y., Zheng, W., Zhang, Y., Zhou, J., Lu, J.: Tri-perspective view for vision-based 3d semantic occupancy prediction. In: CVPR. pp. 9223–9232 (2023)
33. IDEA-Research: Grounded segment anything. <https://github.com/IDEA-Research/Grounded-Segment-Anything>
34. Kerbl, B., Kopanas, G., Leimkühler, T., Drettakis, G.: 3d gaussian splatting for real-time radiance field rendering. *TOG* **42**(4), 1–14 (2023)
35. Kim, J.H., Hur, J., Nguyen, T.P., Jeong, S.G.: Self-supervised surround-view depth estimation with volumetric feature fusion. *NeurIPS* **35**, 4032–4045 (2022)
36. Kirillov, A., Mintun, E., Ravi, N., Mao, H., Rolland, C., Gustafson, L., Xiao, T., Whitehead, S., Berg, A.C., Lo, W.Y., et al.: Segment anything. In: ICCV (2023)
37. Klodt, M., Vedaldi, A.: Supervising the new with the old: learning SFM from SFM. In: ECCV. pp. 698–713 (2018)
38. Lee, J.H., Han, M.K., Ko, D.W., Suh, I.H.: From big to small: Multi-scale local planar guidance for monocular depth estimation. arXiv preprint arXiv:1907.10326 (2019)

39. Li, J., Feng, Z., She, Q., Ding, H., Wang, C., Lee, G.H.: Mine: Towards continuous depth mpi with nerf for novel view synthesis. In: Proceedings of the IEEE/CVF International Conference on Computer Vision. pp. 12578–12588 (2021)
40. Li, J., Han, K., Wang, P., Liu, Y., Yuan, X.: Anisotropic convolutional networks for 3d semantic scene completion. In: Proceedings of the IEEE/CVF Conference on Computer Vision and Pattern Recognition. pp. 3351–3359 (2020)
41. Li, Y., Li, S., Liu, X., Gong, M., Li, K., Chen, N., Wang, Z., Li, Z., Jiang, T., Yu, F., et al.: Sscbench: A large-scale 3d semantic scene completion benchmark for autonomous driving. arXiv preprint arXiv:2306.09001 (2023)
42. Li, Y., Yu, Z., Choy, C., Xiao, C., Alvarez, J.M., Fidler, S., Feng, C., Anandkumar, A.: Voxformer: Sparse voxel transformer for camera-based 3d semantic scene completion. In: CVPR. pp. 9087–9098 (2023)
43. Li, Y., Ge, Z., Yu, G., Yang, J., Wang, Z., Shi, Y., Sun, J., Li, Z.: Bevdepth: Acquisition of reliable depth for multi-view 3d object detection. arXiv preprint arXiv:2206.10092 (2022)
44. Li, Z., Niklaus, S., Snavely, N., Wang, O.: Neural scene flow fields for space-time view synthesis of dynamic scenes. In: CVPR. pp. 6498–6508 (2021)
45. Li, Z., Wang, W., Li, H., Xie, E., Sima, C., Lu, T., Yu, Q., Dai, J.: Bevformer: Learning bird’s-eye-view representation from multi-camera images via spatiotemporal transformers. In: ECCV (2022)
46. Li, Z., Yu, Z., Austin, D., Fang, M., Lan, S., Kautz, J., Alvarez, J.M.: Fb-occ: 3d occupancy prediction based on forward-backward view transformation. arXiv preprint arXiv:2307.01492 (2023)
47. Li, Z., Yu, Z., Wang, W., Anandkumar, A., Lu, T., Alvarez, J.M.: Fb-bev: Bev representation from forward-backward view transformations. In: ICCV. pp. 6919–6928 (2023)
48. Liang, T., Xie, H., Yu, K., Xia, Z., Lin, Z., Wang, Y., Tang, T., Wang, B., Tang, Z.: Bevfusion: A simple and robust lidar-camera fusion framework. arXiv preprint arXiv:2205.13790 (2022)
49. Lin, C.H., Ma, W.C., Torralba, A., Lucey, S.: Barf: Bundle-adjusting neural radiance fields. In: ICCV. pp. 5741–5751 (2021)
50. Liu, F., Shen, C., Lin, G., Reid, I.: Learning depth from single monocular images using deep convolutional neural fields. TPAMI **38**(10), 2024–2039 (2015)
51. Liu, S., Zeng, Z., Ren, T., Li, F., Zhang, H., Yang, J., Li, C., Yang, J., Su, H., Zhu, J., et al.: Grounding dino: Marrying dino with grounded pre-training for open-set object detection. arXiv preprint arXiv:2303.05499 (2023)
52. Liu, Y., Wang, T., Zhang, X., Sun, J.: Petr: Position embedding transformation for multi-view 3d object detection. arXiv preprint arXiv:2203.05625 (2022)
53. Liu, Z., Tang, H., Amini, A., Yang, X., Mao, H., Rus, D., Han, S.: Bevfusion: Multi-task multi-sensor fusion with unified bird’s-eye view representation. arXiv preprint arXiv:2205.13542 (2022)
54. Lu, C., van de Molengraft, M.J.G., Dubbelman, G.: Monocular semantic occupancy grid mapping with convolutional variational encoder–decoder networks. IEEE Robotics and Automation Letters **4**(2), 445–452 (2019)
55. Mahjourian, R., Wicke, M., Angelova, A.: Unsupervised learning of depth and ego-motion from monocular video using 3d geometric constraints. In: CVPR. pp. 5667–5675 (2018)
56. Martin-Brualla, R., Radwan, N., Sajjadi, M.S., Barron, J.T., Dosovitskiy, A., Duckworth, D.: Nerf in the wild: Neural radiance fields for unconstrained photo collections. In: CVPR. pp. 7210–7219 (2021)

57. Max, N.: Optical models for direct volume rendering. *IEEE Transactions on Visualization and Computer Graphics* **1**(2), 99–108 (1995)
58. Mildenhall, B., Hedman, P., Martin-Brualla, R., Srinivasan, P.P., Barron, J.T.: Nerf in the dark: High dynamic range view synthesis from noisy raw images. In: *CVPR*. pp. 16190–16199 (2022)
59. Mildenhall, B., Srinivasan, P.P., Tancik, M., Barron, J.T., Ramamoorthi, R., Ng, R.: Nerf: Representing scenes as neural radiance fields for view synthesis. In: *ECCV*. pp. 405–421. Springer (2020)
60. Müller, T., Evans, A., Schied, C., Keller, A.: Instant neural graphics primitives with a multiresolution hash encoding. *TOG* **41**(4), 1–15 (2022)
61. Niemeyer, M., Geiger, A.: Giraffe: Representing scenes as compositional generative neural feature fields. In: *CVPR*. pp. 11453–11464 (2021)
62. Oechsle, M., Peng, S., Geiger, A.: Unisurf: Unifying neural implicit surfaces and radiance fields for multi-view reconstruction. In: *ICCV*. pp. 5589–5599 (2021)
63. Pan, M., Liu, J., Zhang, R., Huang, P., Li, X., Liu, L., Zhang, S.: Renderocc: Vision-centric 3d occupancy prediction with 2d rendering supervision. In: *ICRA* (2024)
64. Park, K., Sinha, U., Barron, J.T., Bouaziz, S., Goldman, D.B., Seitz, S.M., Martin-Brualla, R.: Nerfies: Deformable neural radiance fields. In: *ICCV*. pp. 5865–5874 (2021)
65. Pumarola, A., Corona, E., Pons-Moll, G., Moreno-Noguer, F.: D-nerf: Neural radiance fields for dynamic scenes. In: *CVPR*. pp. 10318–10327 (2021)
66. Ranjan, A., Jampani, V., Balles, L., Kim, K., Sun, D., Wulff, J., Black, M.J.: Competitive Collaboration: Joint Unsupervised Learning of Depth, Camera Motion, Optical Flow and Motion Segmentation. In: *CVPR*. pp. 12240–12249 (2019)
67. Reiser, C., Peng, S., Liao, Y., Geiger, A.: Kilonerf: Speeding up neural radiance fields with thousands of tiny mlps. In: *ICCV*. pp. 14335–14345 (2021)
68. Roldao, L., de Charette, R., Verroust-Blondet, A.: Lmscnet: Lightweight multi-scale 3d semantic completion. In: *2020 International Conference on 3D Vision (3DV)*. pp. 111–119. IEEE (2020)
69. Roy, A., Todorovic, S.: Monocular depth estimation using neural regression forest. In: *CVPR*. pp. 5506–5514 (2016)
70. Schmied, A., Fischer, T., Danelljan, M., Pollefeys, M., Yu, F.: R3d3: Dense 3d reconstruction of dynamic scenes from multiple cameras. In: *ICCV*. pp. 3216–3226 (2023)
71. Shen, T., Luo, Z., Zhou, L., Deng, H., Zhang, R., Fang, T., Quan, L.: Beyond Photometric Loss for Self-Supervised Ego-Motion Estimation. *arXiv preprint arXiv:1902.09103* (2019)
72. Shen, T., Zhou, L., Luo, Z., Yao, Y., Li, S., Zhang, J., Fang, T., Quan, L.: Self-Supervised Learning of Depth and Motion Under Photometric Inconsistency. In: *ICCVW*. pp. 0–0 (2019)
73. Shi, Y., Cai, H., Ansari, A., Porikli, F.: Ega-depth: Efficient guided attention for self-supervised multi-camera depth estimation. In: *CVPRW*. pp. 119–129 (2023)
74. Srinivasan, P.P., Deng, B., Zhang, X., Tancik, M., Mildenhall, B., Barron, J.T.: Nerv: Neural reflectance and visibility fields for relighting and view synthesis. In: *CVPR*. pp. 7495–7504 (2021)
75. Sun, C., Sun, M., Chen, H.T.: Direct voxel grid optimization: Super-fast convergence for radiance fields reconstruction. In: *CVPR*. pp. 5459–5469 (2022)
76. Tancik, M., Casser, V., Yan, X., Pradhan, S., Mildenhall, B., Srinivasan, P.P., Barron, J.T., Kretzschmar, H.: Block-nerf: Scalable large scene neural view synthesis. In: *CVPR*. pp. 8248–8258 (2022)

77. Tian, X., Jiang, T., Yun, L., Wang, Y., Wang, Y., Zhao, H.: Occ3d: A large-scale 3d occupancy prediction benchmark for autonomous driving. arXiv preprint arXiv:2304.14365 (2023)
78. Tong, W., Sima, C., Wang, T., Chen, L., Wu, S., Deng, H., Gu, Y., Lu, L., Luo, P., Lin, D., et al.: Scene as occupancy. In: ICCV. pp. 8406–8415 (2023)
79. Tosi, F., Aleotti, F., Poggi, M., Mattoccia, S.: Learning monocular depth estimation infusing traditional stereo knowledge. In: CVPR. pp. 9799–9809 (2019)
80. Tretschk, E., Tewari, A., Golyanik, V., Zollhöfer, M., Lassner, C., Theobalt, C.: Non-rigid neural radiance fields: Reconstruction and novel view synthesis of a dynamic scene from monocular video. In: ICCV. pp. 12959–12970 (2021)
81. Wang, C., Miguel Buenaposada, J., Zhu, R., Lucey, S.: Learning depth from monocular videos using direct methods. In: CVPR. pp. 2022–2030 (2018)
82. Wang, P., Liu, L., Liu, Y., Theobalt, C., Komura, T., Wang, W.: Neus: Learning neural implicit surfaces by volume rendering for multi-view reconstruction. *NeurIPS* **34**, 27171–27183 (2021)
83. Wang, X., Zhu, Z., Xu, W., Zhang, Y., Wei, Y., Chi, X., Ye, Y., Du, D., Lu, J., Wang, X.: Openoccupancy: A large scale benchmark for surrounding semantic occupancy perception. In: ICCV (2023)
84. Wang, Z., Wu, S., Xie, W., Chen, M., Prisacariu, V.A.: Nerf-: Neural radiance fields without known camera parameters. arXiv preprint arXiv:2102.07064 (2021)
85. Watson, J., Firman, M., Brostow, G.J., Turmukhambetov, D.: Self-Supervised Monocular Depth Hints. In: ICCV. pp. 2162–2171 (2019)
86. Wei, Y., Liu, S., Rao, Y., Zhao, W., Lu, J., Zhou, J.: Nerfingmvs: Guided optimization of neural radiance fields for indoor multi-view stereo. In: ICCV. pp. 5610–5619 (2021)
87. Wei, Y., Zhao, L., Zheng, W., Zhu, Z., Rao, Y., Huang, G., Lu, J., Zhou, J.: Surrounddepth: Entangling surrounding views for self-supervised multi-camera depth estimation. In: CoRL. pp. 539–549. PMLR (2023)
88. Wei, Y., Zhao, L., Zheng, W., Zhu, Z., Zhou, J., Lu, J.: Surroundocc: Multi-camera 3d occupancy prediction for autonomous driving. In: ICCV. pp. 21729–21740 (2023)
89. Xu, J., Liu, X., Bai, Y., Jiang, J., Wang, K., Chen, X., Ji, X.: Multi-camera collaborative depth prediction via consistent structure estimation. In: ACM-MM. pp. 2730–2738 (2022)
90. Xu, Q., Xu, Z., Philip, J., Bi, S., Shu, Z., Sunkavalli, K., Neumann, U.: Point-nerf: Point-based neural radiance fields. In: CVPR. pp. 5438–5448 (2022)
91. Yariv, L., Gu, J., Kasten, Y., Lipman, Y.: Volume rendering of neural implicit surfaces. *NeurIPS* **34**, 4805–4815 (2021)
92. Yin, Z., Shi, J.: Geonet: Unsupervised learning of dense depth, optical flow and camera pose. In: CVPR. pp. 1983–1992 (2018)
93. Yu, Z., Peng, S., Niemeyer, M., Sattler, T., Geiger, A.: Monosdf: Exploring monocular geometric cues for neural implicit surface reconstruction. *NeurIPS* **35**, 25018–25032 (2022)
94. Yu, Z., Shu, C., Deng, J., Lu, K., Liu, Z., Yu, J., Yang, D., Li, H., Chen, Y.: Flashocc: Fast and memory-efficient occupancy prediction via channel-to-height plugin. arXiv preprint arXiv:2311.12058 (2023)
95. Zhang, K., Riegler, G., Snavely, N., Koltun, V.: Nerf++: Analyzing and improving neural radiance fields. arXiv preprint arXiv:2010.07492 (2020)
96. Zhang, Y., Zhu, Z., Du, D.: Occformer: Dual-path transformer for vision-based 3d semantic occupancy prediction. In: ICCV (2023)

97. Zhang, Y., Zhu, Z., Zheng, W., Huang, J., Huang, G., Zhou, J., Lu, J.: Beverage: Unified perception and prediction in birds-eye-view for vision-centric autonomous driving. arXiv preprint arXiv:2205.09743 (2022)
98. Zhang, Z., Xu, C., Yang, J., Gao, J., Cui, Z.: Progressive hard-mining network for monocular depth estimation. *TIP* **27**(8), 3691–3702 (2018)
99. Zhou, J., Wang, Y., Qin, K., Zeng, W.: Moving Indoor: Unsupervised Video Depth Learning in Challenging Environments. In: *ICCV*. pp. 8618–8627 (2019)
100. Zhou, T., Brown, M., Snavely, N., Lowe, D.G.: Unsupervised learning of depth and ego-motion from video. In: *CVPR*. pp. 1851–1858 (2017)
101. Zou, Y., Luo, Z., Huang, J.B.: Df-net: Unsupervised joint learning of depth and flow using cross-task consistency. In: *ECCV*. pp. 36–53 (2018)
102. Zuo, S., Zheng, W., Huang, Y., Zhou, J., Lu, J.: Pointocc: Cylindrical tri-perspective view for point-based 3d semantic occupancy prediction. arXiv preprint arXiv:2308.16896 (2023)

Appendix

A Parameterized Occupancy Fields Derivation

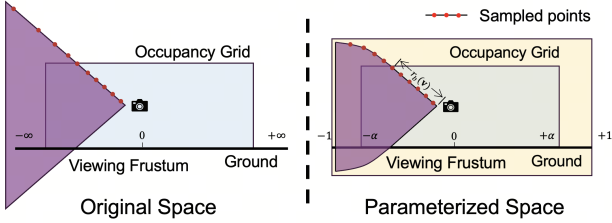


Fig. A: Comparison between original space and parameterized space. The original space utilizes the conventional Euclidean space, emphasizing linear mapping. The parameterized space is divided into two parts: an inner space with linear mapping to preserve high-resolution detail and an outer space where point distribution is scaled inversely with distance, facilitating the representation of an infinite range within a finite spatial domain.

The objective of utilizing parameterized coordinates is to encapsulate an infinite range within a confined spatial domain. This concept is illustrated in Fig. A, where the spatial domain is bifurcated into two distinct regions: the inner space and the outer space. The inner space retains a linear mapping to ensure the preservation of high-resolution details. Conversely, in the outer space, point distribution is executed in proportion to disparity, which inversely relates to distance. Consequently, the transformation function is articulated as follows:

$$f(r) = \begin{cases} \alpha \cdot r' & |r'| \leq 1 \\ \frac{r'}{|r'|} \cdot \left(1 - \frac{a}{|r'|+b}\right) & |r'| > 1 \end{cases}, \quad (10)$$

where $r' = r/r_b$ denotes the normalized coordinate based on the input r . The parameters a and b are introduced to maintain the continuity of the first derivative. The determination of these parameters is achieved through the resolution of the ensuing equations:

$$\begin{cases} \lim_{r \rightarrow r_b^+} f(r) = \lim_{r \rightarrow r_b^-} f(r) \\ \lim_{r \rightarrow r_b^+} f'(r) = \lim_{r \rightarrow r_b^-} f'(r) \end{cases}, \quad (11)$$

The derived solutions are presented as:

$$\begin{cases} a = \frac{(1-\alpha)^2}{\alpha} \\ b = \frac{1-2\alpha}{\alpha} \end{cases}. \quad (12)$$

Table A: Details of prompt strategy.

Original labels	Ours
car	sedan
bicycle	bicycle bicyclist
vegetation	tree
motorcycle	motorcycle motorcyclist
drivable surface	highway
traffic cone	cone
construction vehicle	crane
manmade	building compound bridge pole billboard light ashbin

B Semantic Label Generation Details

In Section 3.4 of main paper, we present a concise overview of the generation of semantic labels using our open-vocabulary model, Grounded-SAM [33, 36, 51]. We employ three prompt strategies to manually refine the category names fed into Grounding DINO [51]. To illustrate these strategies, we focus on the semantic labels for occupancy in the Occ3D-nuScenes [77] benchmark and provide a detailed explanation.

Specifically, for the synonymous substitution strategy, we substitute ‘car’ with ‘sedan’ to enhance model discrimination, replace ‘vegetation’ with ‘tree’ to improve detection rates, and change ‘driveable surface’ to ‘highway’ to aid the model in distinguishing it from ‘sidewalk’. In the case of splitting the word strategy, we change ‘manmade’ to ‘building’, ‘compound’, ‘bridge’, ‘pole’, ‘billboard’, ‘light’, and ‘ashbin’, among others. Moreover, we employ the incorporating additional information strategy, introducing prompts such as ‘bicyclist’, ‘motorcyclist’, and ‘barricade’. Finally, we modify ‘traffic cone’ to ‘cone’ and ‘construction vehicle’ to ‘crane’ due to the bad performance of Grounding DINO [51] when processing original phrases. Readers can refer to Table A for our prompts replacement. For hyperparameter, we set both ‘BOX_THRESHOLD’ and ‘TEXT_THRESHOLD’ of Grounding DINO [51] to 0.20. We find that the open-vocabulary model has difficulty to deal with long prompts. Thus, we further organize our refined prompts into several groups instead of feeding them together, allowing our open-vocabulary model to generate detection frames for each group sequentially.

C Evaluation Metrics

The detailed evaluation metrics of self-supervised depth estimation can be described as follows:

$$- \text{Abs Rel: } \frac{1}{|T|} \sum_{d \in T} |d - d^*|/d^*,$$

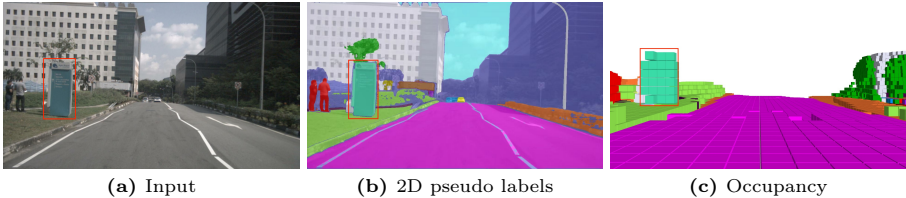


Fig. B: Given the prompt 'billboard', our model can predict related occupancy, which is not present in the official annotations.

- Sq Rel: $\frac{1}{|T|} \sum_{d \in T} |d - d^*|^2 / d^*$,
- RMSE: $\sqrt{\frac{1}{|T|} \sum_{d \in T} |d - d^*|^2}$,
- RMSE log: $\sqrt{\frac{1}{|T|} \sum_{d \in T} |\log d - \log d^*|^2}$,
- $\delta < t$: % of d s.t. $\max(\frac{d}{d^*}, \frac{d^*}{d}) = \delta < t$,

where d and d^* indicate predicted and ground truth depths respectively, and T indicates all pixels on the depth image D . In our experiments, all the predicted depth maps are scale-aware and we do not perform any scale alignment.

D The benefits of open-vocabulary

Fig. B shows that the open-vocabulary model have the ability to generate results of undefined categories in nuScenes dataset. In this way, our method can be extended to arbitrary classes and applied to both public and internally collected datasets. Also, it is potential to generalize to the rare classes (corner cases), which is critical in autonomous driving. In contrast, the trivial segmentation model pre-trained on nuScenes dataset is restricted to the pre-defined classes and will violate to self-supervised setting.

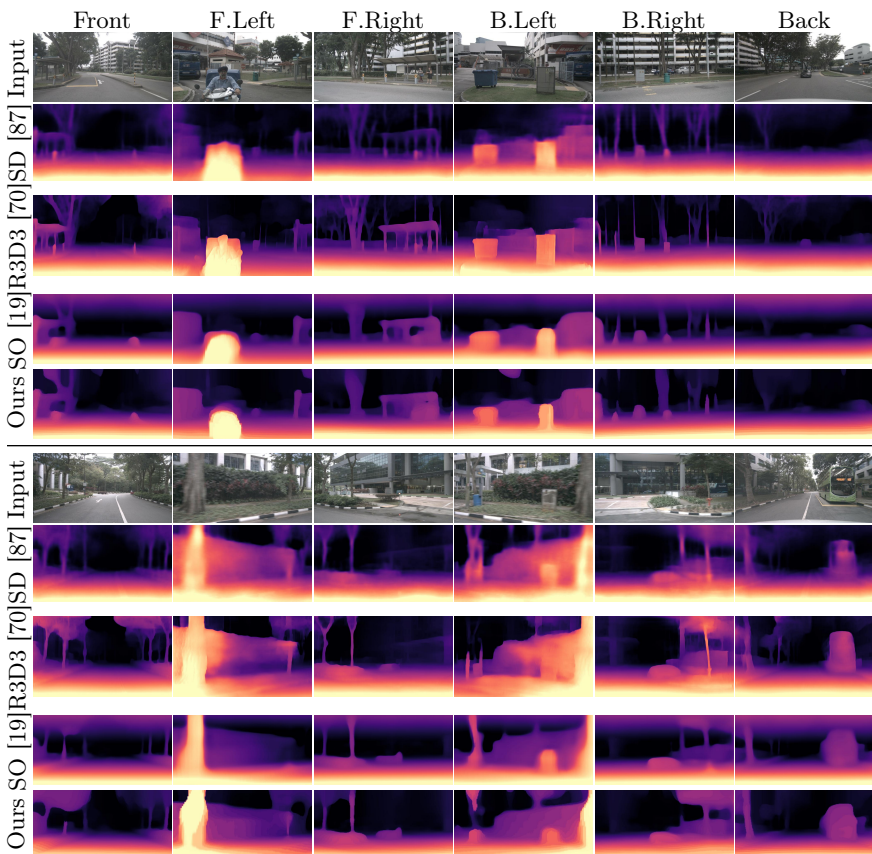
E More Experimental Results

Per-camera evaluation: We give the per-camera comparisons of our method with previous works on the nuScenes [8] dataset in Table B. Our method outperforms other methods across all cameras, with a particularly high improvement in side views.

Qualitative Comparisons: Fig. C shows qualitative comparisons on nuScenes [8] validation set. We visualize several state-of-the-art depth estimation and occupancy prediction methods' results with their official codes. Compared with the these methods, our occupancy-based method has fewer artifacts and better overall accuracy.

Table B: Per-camera comparisons for scale-aware multi-camera depth estimation on the nuScenes dataset. Tests are conducted within 80 meters.

Method	Abs Rel ↓					
	Front	F.Left	F.Right	B.Left	B.Right	Back
FSM [26]	0.186	0.287	0.375	0.296	0.418	0.221
SurroundDepth [87]	0.179	0.260	0.340	0.282	0.403	0.212
R3D3 [70]	0.174	0.230	0.302	0.249	0.360	0.201
Ours	0.132	0.190	0.227	0.204	0.289	0.169

**Fig. C:** Qualitative comparison on the nuScenes dataset. **Better viewed when zoomed in.**